Nano Research 2016, 9(11): 3229–3246
DOI 10.1007/s12274-016-1201-z
Research Article

ISSN 1998-0124
CN 11-5974/O4

Cadmium nanoclusters in a protein matrix: Synthesis, characterization, and application in targeted drug delivery and cellular imaging

Morteza Sarparast[1,§], Abolhassan Noori[1,§], Hoda Ilkhani[1], S. Zahra Bathaie[2], Maher F. El-Kady[3,4], Lisa J. Wang[3], Huong Pham[3], Kristofer L. Marsh[3], Richard B. Kaner[3,5] (✉), and Mir F. Mousavi[1,3] (✉)

[1] *Department of Chemistry, Tarbiat Modares University, Tehran 14115-175, Iran*
[2] *Department of Clinical Biochemistry, Faculty of Medical Sciences, Tarbiat Modares University, Tehran 14115-111, Iran*
[3] *Department of Chemistry and Biochemistry, University of California, Los Angeles, Los Angeles, CA 90095, USA*
[4] *Department of Chemistry, Faculty of Science, Cairo University, Giza 12613, Egypt*
[5] *California NanoSystems Institute, University of California, Los Angeles, Los Angeles, CA 90095, USA*
[§] *These authors contributed equally to this work.*

Received: 24 April 2016
Revised: 2 July 2016
Accepted: 4 July 2016

KEYWORDS

Cd nanoclusters, hyaluronic acid, targeted drug delivery, fluorescence bioimaging, nanocarrier

ABSTRACT

Biotemplated metal nanoclusters have garnered much attention owing to their wide range of potential applications in biosensing, bioimaging, catalysis, and nanomedicine. Here, we report the synthesis of stable, biocompatible, water-soluble, and highly fluorescent bovine serum albumin-templated cadmium nanoclusters (Cd_{NCs}) through a facile one-pot green method. We covalently conjugated hyaluronic acid (HA) to the Cd_{NCs} to form a pH-responsive, tumor-targeting theranostic nanocarrier with a sustained release profile for doxorubicin (DOX), a model anticancer drug. The nanocarrier showed a DOX encapsulation efficiency of about 75.6%. DOX release profiles revealed that 74% of DOX was released at pH 5.3, while less than 26% of DOX was released at pH 7.4 within the same 24-h period. The nanocarrier selectively recognized MCF-7 breast cancer cells expressing CD44, a cell surface receptor for HA, whereas no such recognition was observed with HA receptor-negative HEK293 cells. Biocompatibility of the nanocarrier was evaluated through cytotoxicity assays with HEK293 and MCF-7 cells. The nanocarrier exhibited very low to no cytotoxicity, whereas the DOX-loaded nanocarrier showed considerable cellular uptake and enhanced MCF-7 breast cancer cell-killing ability. We also confirmed the feasibility of using the highly fluorescent nanoconjugate for bioimaging of MCF-7 and HeLa cells. The superior targeted drug delivery efficacy, cellular imaging capability, and low cytotoxicity position this nanoconjugate as an exciting new nanoplatform with promising biomedical applications.

Address correspondence to Richard B. Kaner, kaner@chem.ucla.edu; Mir F. Mousavi, mousavim@modares.ac.ir

1 Introduction

Nanostructured materials have attracted considerable attention over the past few decades because of their distinctive size-dependent physicochemical properties [1]. Metal [2], metal oxide [3], and semiconductor [4] nanoparticles as well as polymeric [5–7], organic, biomolecular, and carbon-based [8] nanostructures are promising platforms for a wide variety of applications ranging from biosensing [9–12], catalysis [13, 14], biomedicine [15, 16], and electronics [17, 18] to energy storage [19]. Among these platforms, metal nanoclusters (M_{NCs}) or quantum clusters, which are atomically precise particles consisting of a few to roughly tens of metal atoms, have attracted particular interest because of their unique properties and potential applications [20]. Quantum confinement of the electrons in M_{NCs}, which have a size comparable to the Fermi wavelength of an electron (<2 nm), provides them with fascinating molecule-like properties such as quantized energy states (HOMO-LUMO transition of electrons), vanishing surface plasmon resonance, optical chirality, magnetism, and wavelength-tunable (size-dependent) fluorescence [21–23]. The distinctive features of M_{NCs} render them appropriate for many cutting-edge applications in catalysis, optoelectronics, biosensing, targeted drug delivery, and bioimaging [24–27]. However, bare M_{NCs} are thermodynamically unstable owing to excess surface energy and tend to agglomerate in liquid media in the absence of protective ligands. Thus, a large number of protective ligands, such as thiolates [28, 29], phosphines [20, 30], dendrimers [20, 31], DNA [32, 33], peptides [34, 35], and more recently proteins, as new entries in this field, have been reported [36, 37]. Though the field of protein-templated metal and metal-alloy NCs has just started to flourish, in recent years, there has been extensive research on luminescent protein-templated NCs using various proteins, such as bovine serum albumin (BSA), lysozyme, trypsin, pepsin, and hemoglobin [38–42]. Using a protein as a template or scaffold for the synthesis of M_{NCs} provides many advantages, such as excellent stability, low toxicity, good water solubility, and biocompatibility [40, 43–45]. Furthermore, the protein coating on M_{NCs} is rich in various functional groups, which simplifies post-modifications of NCs for biological and biomedical applications [46, 47]. Because of these fascinating properties, protein-templated M_{NCs} can be excellent substitutes for other bioimaging agents, such as fluorescent quantum dots (QDs). QDs have some positive aspects, including size-dependent fluorescence emission, high quantum yield (QY), large Stokes shift, and high photostability, but they also have some drawbacks. Although controversial in some cases, the disadvantages of QDs include (1) cytotoxicity; (2) a tendency to self-aggregate inside living cells as well as the extracellular space [48, 49]; (3) the necessity of surface functionalization for subsequent biomedical applications; and (4) the use of toxic, air-sensitive, and expensive chemicals (such as trioctylphosphine oxide), high temperatures, and nonpolar organic solvents in their synthesis [50]. Although the size of QDs has been reduced to <5 nm, allowing efficient renal clearance, these state-of-the-art materials still suffer from the inherent toxicity of heavy metals. Even at lower concentrations, this toxicity has restrained the biomedical applications of QDs [37, 51]. Noble M_{NCs}, such as Au_{NCs} and Ag_{NCs}, are the most extensively investigated category of NCs because of their facile synthesis, excellent biocompatibility, and good stability [41]. More recently, NCs of Fe, Ni, Cu, and Pt have also been synthesized [22, 40, 52–54]. Cadmium nanoclusters have excellent fluorescence properties that make them very useful for biosensing, drug delivery, and cellular imaging. To date, few experimental studies have provided direct insight into the synthesis of Cd_{NCs}. This is because of the difficulty of reducing Cd ions ($E^\circ_{Cd^{2+}/Cd} = -0.402$ V) in comparison with Au ($E^\circ_{Au^{+}/Au} = 1.83$ V) and Ag ($E^\circ_{Ag^{+}/Ag} = 0.799$ V) ions. This explains why there has been limited progress in the development of biotemplated aqueous-phase synthetic methods for the preparation of Cd_{NCs}. Another challenge that restricts the application of Cd_{NCs} is the inherent toxicity of cadmium, which can be a major issue if leakage occurs. When NCs are stabilized with small biomolecules, oxidizing agents or irradiation can trigger leakage of the metal ions. Therefore, very stable, highly luminescent, biocompatible Cd_{NCs} with visible-range fluorescence need to be synthesized to provide a substitute for toxic Cd QDs in bioimaging of living cells and targeted therapeutics.

For M_{NCs} to be applicable in drug delivery and bioimaging, ligands are required to provide tumor cell specificity. Different tumor-recognition moieties have been used for targeted drug delivery. Folic acid, one of the most widely used and efficient targeting moieties, has a low cost but is limited by its poor water solubility. Antibodies show high selectivity (and sometimes specificity) for their target, but they are expensive and may have side effects. Peptides are cost-effective but have a limited range of target cell types. Among all the possibilities, hyaluronic acid (HA) is one of the most economical and efficient targeting moieties for cancer therapy. Many types of tumor cells overexpress HA receptors such as the receptor for hyaluronate-mediated motility (RHAMM) and cluster of differentiation 44 (CD44) [55]. HA is a biodegradable, biocompatible, ubiquitous, and non-immunogenic linear polysaccharide that has been used successfully in a variety of biomedical applications, including molecular imaging, drug delivery, and tissue engineering [56]. Because HA has multiple functional groups (such as –COOH and –OH), it can be easily conjugated to anticancer drugs or nanocarriers of drugs or genes such as protein-templated NCs, the surface of which is rich in amino groups [57]. HA-directed delivery systems preserve cell viability and show high HA receptor-mediated endocytic cellular uptake [58, 59]. To date, there are only a few reports on HA-conjugated magnetic NCs or nanocrystals targeting cancer cells overexpressing CD44, and these have been used as contrast agents for magnetic resonance imaging [60, 61].

In this work, we synthesized water-soluble Cd_{NCs} with low toxicity and bright and stable fluorescence by a simple and green chemical method, using BSA as both the reducing and stabilizing agent (Scheme 1). To investigate the suitability of the Cd_{NCs} for cancer cell imaging as well as targeted drug delivery, we conjugated the as-synthesized Cd_{NCs} to HA, creating a carrier for the anticancer drug doxorubicin (DOX) that targets cancer cells overexpressing CD44 (Scheme 1). *In vitro* cell viability studies carried out with human breast cancer (MCF-7) and human embryonic kidney (HEK293) cells confirmed the noncytotoxic nature of the BSA-stabilized Cd_{NCs} and their suitability for biological applications.

2 Experimental

2.1 Materials

All reagents were of analytical grade and were used without further purification. $CdCl_2$, NaOH, NaCl, KCl, $MgCl_2$, $CaCl_2$, and H_2O_2 were obtained from Merck (Darmstadt, Germany). BSA, N-(3-dimethylaminopropyl)-N′-ethylcarbodiimide hydrochloride (EDC), and N-hydroxysuccinimide (NHS) were purchased from Sigma. DOX was obtained from the Iranian Red Crescent Society. Sodium hyaluronate, a sodium salt of HA (M_W = 100–120 kDa), was obtained from Lifecore Biomedical. All stock solutions were prepared using deionized water with a resistivity close to 18 MΩ·cm.

2.2 Apparatus

UV–vis absorption measurements were performed with a UV S-2100 spectrophotometer (Scinco, Korea), and spectrofluorimetric measurements were performed in the range of 280–700 nm with an LS-50B spectrophotometer equipped with a xenon lamp as the excitation source (Perkin-Elmer Inc., USA). The bandpass for excitation and emission beams was set at 15 and 20 nm, respectively. Far-UV circular dichroism (CD) spectra were obtained using a J-810 spectropolarimeter (Jasco, Victoria, Canada) connected to a Jasco water bath. All spectra were recorded at intervals of 1 nm between 190 and 250 nm, a response time of 4 s, and a scan rate of 100 nm/min. Each spectrum was an average of four scans, with a baseline scan subtracted. In all cases, the spectrum was recorded using a 0.0125 mg/mL protein solution. The zeta (ζ) potential and hydrodynamic diameter of the Cd_{NCs} were measured by dynamic light scattering using a Zetasizer Nano ZS instrument (Malvern Instruments Ltd., Malvern, Worcestershire, UK) at a Cd_{NC} concentration of 0.5 mg/mL in deionized water. The data are reported as the mean ± standard deviation (n = 3). For Fourier transform infrared (FT-IR) spectroscopy, samples were lyophilized, mixed with KBr to make pellets, and analyzed using a Perkin-Elmer spectrophotometer

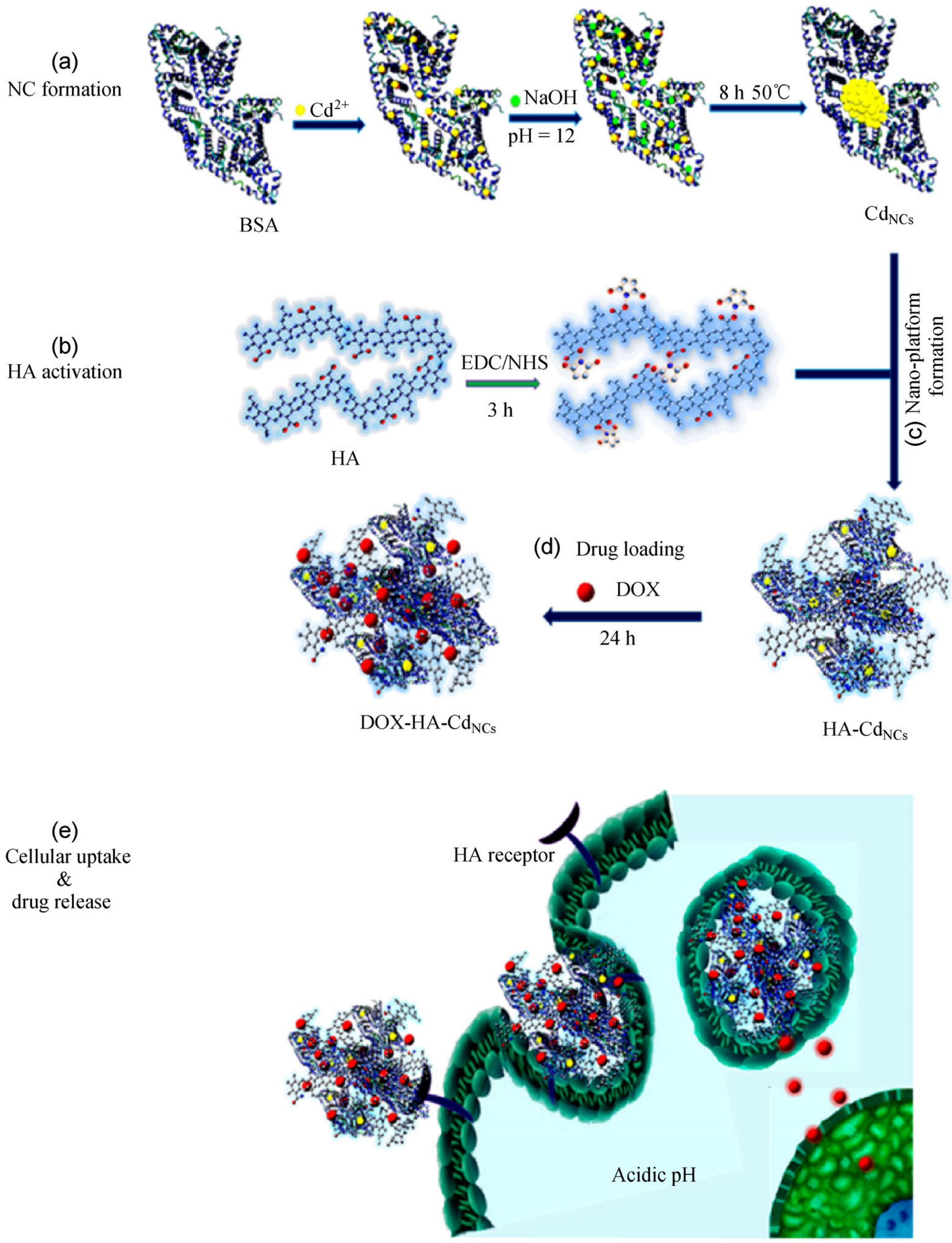

Scheme 1 Schematic illustration of the synthesis of Cd_{NCs} (a), conjugation of HA to Cd_{NCs} (HA-Cd_{NCs}) (b) and (c), DOX loading into the HA-Cd_{NC} nanocarrier (DOX-HA-Cd_{NCs}) (d), and HA receptor-mediated targeted drug delivery (e).

(Perkin-Elmer Inc., USA) in the range of 4,000–400 cm^{-1}. The morphology and structure of the as-synthesized Cd_{NCs} were examined by high-resolution transmission electron microscopy (HR-TEM) using a T20 iCorr transmission electron microscope (FEI, USA) operating at an accelerating voltage of 200 kV. Samples for HR-TEM were prepared by dropping Cd_{NC} solution onto formvar/carbon-coated copper TEM grids (200 mesh; Ted Pella, USA) and wicking away excess solvent with cellulose filter paper (Whatman). Samples were air-dried overnight and then observed under the microscope. Field-emission scanning electron microscopy (FE-SEM) and energy-dispersive X-ray spectroscopy (EDX) analyses were performed with a Sigma VP instrument (Carl Zeiss, Germany). Typically, 20 μL of sample was drop-cast on a glass slide covered with aluminum foil, air-dried, and sputter-coated with gold film and then analyzed by FE-SEM and EDX. Matrix-assisted laser desorption ionization time-of-flight mass spectrometry (MALDI-TOF MS) spectra of BSA and Cd_{NCs} were recorded using an Applied Biosystems Voyager-DE STR mass spectrometer (UCLA Molecular Instrumentation Center). The spectra collected for Cd_{NCs} at optimized concentrations were smoothed using three-point adjacent averaging in PeakFit software (Systat Software Inc., UK). The shift in the mass spectrum of Cd_{NCs} was compared with the mass of BSA at pH 12 in the presence of 5% NaOH (*v*/*v*). The number of Cd atoms per protein molecule was calculated by subtracting the *m*/*z* value of BSA from that of BSA-templated Cd_{NCs} and dividing the result by the atomic weight of Cd, i.e., 112.4 amu. X-ray photoelectron spectroscopy (XPS) spectra of the samples were recorded using an ESCALab 220I-XL spectrometer (VG, UK). For XPS, lyophilized sample was spotted on carbon tape stuck to the XPS sample plate. Curves were fitted and smoothed using CasaXPS software.

3 Results and discussion

3.1 Synthesis and characterization of fluorescent Cd_{NCs}

Generally, protein-directed synthesis of M_{NCs} entails formation of a metal ion–protein adduct followed by reduction of the metal ions at an elevated pH where the protein acts as both reducing and stabilizing agent [40, 41]. Protein-templated Au_{NCs} can be efficiently synthesized without any extraneous reducing agents. Adopting the same protocol to synthesize Ag_{NCs} is more challenging, and an external reducing agent such as sodium borohydride may be required. Considering the standard reduction potentials of Au^+/Au (1.83 V) and Ag^+/Ag (0.799 V), the impact of the metal ion reduction potential on the efficiency of M_{NC} synthesis is clear. The standard reduction potential of Cd^{2+}/Cd is −0.402 V. Thus, BSA-templated synthesis of Cd_{NCs} is more challenging, and the use of an external reducing agent to facilitate reduction of the metal ions seems unavoidable. Moreover, BSA-templated synthesis of Cd_{NCs} does not necessarily produce fluorescent NCs. Thus, precise control over essential parameters is needed to establish a one-pot method for synthesis of highly fluorescent Cd_{NCs} in an aqueous medium. We investigated the influence of solution pH, reactant ratio, temperature, and incubation time on the fluorescence intensity of as-synthesized Cd_{NCs} at an excitation wavelength of 360 nm and determined the optimal values of these parameters. More details on the optimization are provided in the Electronic Supplementary Material (ESM) (optimization of parameters section and Figs. S1–S4). Under the optimized conditions (pH 12, Cd:BSA molar ratio of 50:3, 50 °C, and 8 h incubation), the fluorescence emission spectrum of Cd_{NCs} excited at 360 nm showed a single band at 475 nm (Fig. 1(a)). We then characterized the synthesized Cd_{NCs} using a variety of spectroscopic and microscopic techniques.

The as-synthesized Cd_{NCs} showed an emission band at 475 nm. However, some oxidative metabolites of protein residues also emit in the blue region. To further assess the formation of Cd_{NCs}, we investigated the fluorescence of BSA in the presence and absence of an oxidizing agent, H_2O_2, as a control experiment (Fig. S5 in the ESM). Under physiological pH, BSA showed a very low-intensity fluorescence close to the emission band of Cd_{NCs}. In addition, the emission of BSA alone showed no significant change in the presence of H_2O_2, whereas H_2O_2 considerably quenched the fluorescence of BSA solution containing Cd ions. These observations ruled out the formation of oxidized adducts of the protein and confirmed the successful formation of fluorescent Cd_{NCs} [54]. Interestingly, we found that the emission of Cd_{NCs} was wavelength tunable, shifting from 420 to 510 nm when the excitation wavelength was tuned from 320 to 390 nm. The tunability of the fluorescence emission of Cd_{NCs} reflects the distribution of Cd_{NCs} with different numbers of constituent Cd atoms (Fig. S6 in the ESM).

UV–vis absorption spectroscopy was also used to verify the *in situ* formation of Cd_{NCs}. The absorption spectra of aqueous solutions of Cd_{NCs} and native BSA are shown in Fig. 1(b). Compared with the spectrum of pure BSA, the Cd_{NCs} spectrum showed a decrease in the absorption band at 285 nm because of changes in the structures of tyrosine (Tyr), tryptophan (Trp),

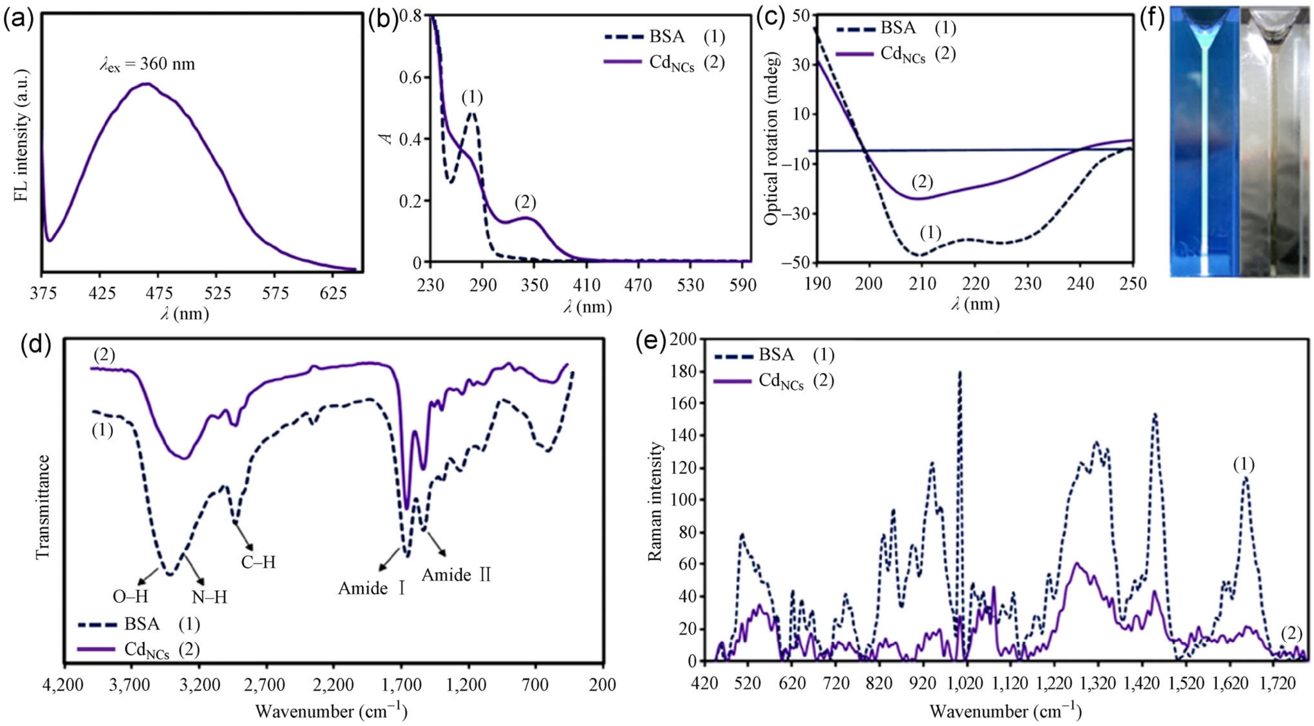

Figure 1 Characterization of Cd_{NCs}. (a) Fluorescence emission spectrum of Cd_{NCs} under excitation at 360 nm. (b) UV–vis absorption spectra of free BSA (1) and Cd_{NCs} (2). (c) CD spectra of free BSA (1) and BSA after Cd_{NCs} formation (2), demonstrating changes in the α-helical content of BSA following NC synthesis. (d) FT-IR spectra of free BSA (1) and BSA after Cd_{NC} formation (2), demonstrating changes in the secondary structure of the protein. (e) Raman spectra of free BSA (1) and Cd_{NCs} (2), showing the role of amino acids such as Phe, Trp, and Tyr as well as functional groups such as carboxyls and thiols in the synthesis of NCs. (f) Photographs of the Cd_{NCs} solution under daylight (1) and UV light (2).

and phenylalanine (Phe) residues [62], which are involved in the reduction of the Cd ions. The clear absorption band appearing at around 350 nm in the spectrum of the final solution confirmed the successful synthesis of Cd_{NCs}.

CD spectroscopy is one of the most efficient methods for scrutinizing changes in the secondary structure of a protein. As shown in Fig. 1(c), the CD spectrum of native BSA has two negative bands at around 208 and 222 nm, indicating an α-helical structure [63]. The formation of Cd_{NCs} resulted in ellipticity at 208 and 222 nm and a blue shift in the band at 208 nm compared with the spectrum of native BSA. These changes reflect a relative decrease of the α-helical content of the protein after NC formation. Using CDNN software, we determined the change in α-helical content to be around 22.2%, which was due to (1) denaturation of the protein under alkaline reaction conditions, (2) formation of a covalent bond between metal (Cd) atoms and electron-rich atoms or groups (e.g., N, O, OH, and NH_2) in the protein, and (3) agglomeration following NC formation at 50 °C. Breakage of some bonds in the native protein, including disulfide bonds [64, 65] owing to the covalent conjugation of Cd to sulfur atoms of BSA residues, may also have changed the secondary and tertiary structures of the protein.

FT-IR spectroscopy is an excellent method for characterizing conformational changes in a protein because the amide bands are sensitive to changes in protein secondary structure [39]. Therefore, FT-IR spectra of BSA were recorded before and after Cd_{NC} formation (Fig. 1(d)). Three amide bands were observed for native BSA, including an amide I band mainly from C=O stretching (1,600–1,700 cm^{-1}), an amide II band assigned to N–H bending and C–N stretching (1,480–1,575 cm^{-1}), and an amide III band arising from the combination of C–N stretching, in-plane C=O bending, and C–C stretching (1,229–1,301 cm^{-1}). The band appearing at 3,400–3,000 cm^{-1} is due to N–H and O–H stretching vibrations [41]. The decrease in the intensity of the bands located at 3,500 and 600 cm^{-1} and the peak shifts in the amide II and III regions suggest nominal changes in the secondary structure of native BSA.

Partial unfolding of native BSA reflects the binding of a metal atom or ion to functional groups of the protein (such as $–NH_2$ and –COOH), facilitating the formation of the NCs [39].

We also studied the formation of NCs using Raman spectroscopy. As shown in Fig. 1(e), there were changes in the intensity or position of the amide I (1,650–1,680 cm^{-1}), amide III (1,200–1,300 cm^{-1}), and skeleton stretching vibration bands (900–1,000 cm^{-1}) in the spectrum of the synthesized product, in comparison with the spectrum of native BSA, providing evidence for the production of Cd_{NCs} and changes in the protein structure. In addition, changes in the peaks of Phe (1,002–1,004 cm^{-1}), Tyr (830–850 cm^{-1}), and Trp (760 and 870–885 cm^{-1}) residues, as well as the –COOH symmetric stretching (1,400–1,405 cm^{-1}) and S–S and C–S stretching (410–680 cm^{-1}) bands, provide evidence for the role of these amino acids in the synthesis of Cd_{NCs} [66].

From the results provided by CD, FT-IR, and Raman spectroscopy, we can conclude that the synthesis of Cd_{NCs} under extremely basic conditions partially changed the secondary structure of BSA. Overall, the similarity of the FT-IR and Raman spectra of free BSA and BSA-templated Cd_{NCs} indicates that the native structure of BSA was mostly retained after encapsulation of metal ions. Preserving the native structure of BSA is very important for subsequent biomedical applications, since an unfolded protein could trigger an immune response. However, although our characterization shows that specific amino acids bear the net negative charge in the synthesis of Cd_{NCs}, the mechanism of action of these amino acids remains unresolved. We hypothesize that the high pH of the reaction solution could make the sulfide groups of BSA available for reaction with the Cd ions, leading to a strong interaction between Cd ions and the sulfur atoms of BSA. Furthermore, similar to the mechanism reported for the synthesis of Au_{NCs}, when the pH exceeds the pK_a of Tyr, the Cd^{2+} ions are reduced to Cd^{+} and subsequently to Cd^0.

The as-obtained Cd_{NCs} solution was pale yellow in visible light and emitted an intense blue-green light (360 nm) under UV illumination (Fig. 1(f)). We used TEM [24], FE-SEM, and MALDI-TOF MS to elucidate the size, morphology, and composition of the as-obtained Cd_{NCs} (Fig. 2). TEM images revealed spherical, uniform, and well-dispersed NCs in the range of 0.6–1.1 nm with an average diameter of 0.9 ± 0.2 nm (Fig. 2(a)). The observed lattice spacing of 0.258 nm agrees well with the separation between the lattice planes of hexagonal Cd (100) [67]. Furthermore, FE-SEM analysis clearly demonstrated the change in morphology of BSA as a capping agent upon formation of Cd_{NCs} (Fig. 2(b) and Figs. S7 and S8 in the ESM). However, the reason for the highly regular arrangement of the atoms requires further consideration. The presence of Cd was also confirmed by EDX spectra of the particles recorded during FE-SEM analysis of the samples (Fig. S9 in the ESM). MALDI-TOF MS was used to identify the number of Cd atoms in the Cd_{NCs}. As shown in Fig. 2(c) and Fig. S10 in the ESM, the MALDI-TOF mass spectrum of BSA shows a peak at 66,950 kDa, whereas the mass spectrum of the Cd_{NCs} shows three distinct peaks at 67,396, 67,957, and 68,854 kDa, which can be assigned to Cd_4, Cd_9, and Cd_{17}, respectively. However, besides Cd_4, Cd_9, and Cd_{17} particles, other adducts with different Cd atom numbers and low signal intensities were also observed. Broadening of mass spectra is quite common in MALDI-TOF MS of M_{NCs} [68]. A jellium model confirmed the numbers of Cd atoms (4, 9, and 17) in the as-synthesized Cd_{NCs} (see the Jellium model section and Fig. S11 in the ESM).

The binding properties and the oxidation state of Cd_{NCs} were determined by XPS (Fig. 2(d)(1)). XPS elemental analysis of the near-surface region of the product showed a double-peak pattern corresponding to Cd $3d_{5/2}$ and Cd $3d_{3/2}$ (the spin-orbit splitting of 3d in Cd) [69]. The chemical states of the Cd atoms were analyzed by deconvolution of the Cd $3d_{5/2}$ and Cd $3d_{3/2}$ bands. As shown in Fig. 2(d)(2), the Cd $3d_{5/2}$ band could be divided into three distinct peaks; the more intense peak at a lower binding energy of 404.67 eV corresponds to Cd–S (the sulfur likely originates from cysteine (Cys) residues of BSA) [70, 71], the peak at a binding energy of 406.2 eV corresponds

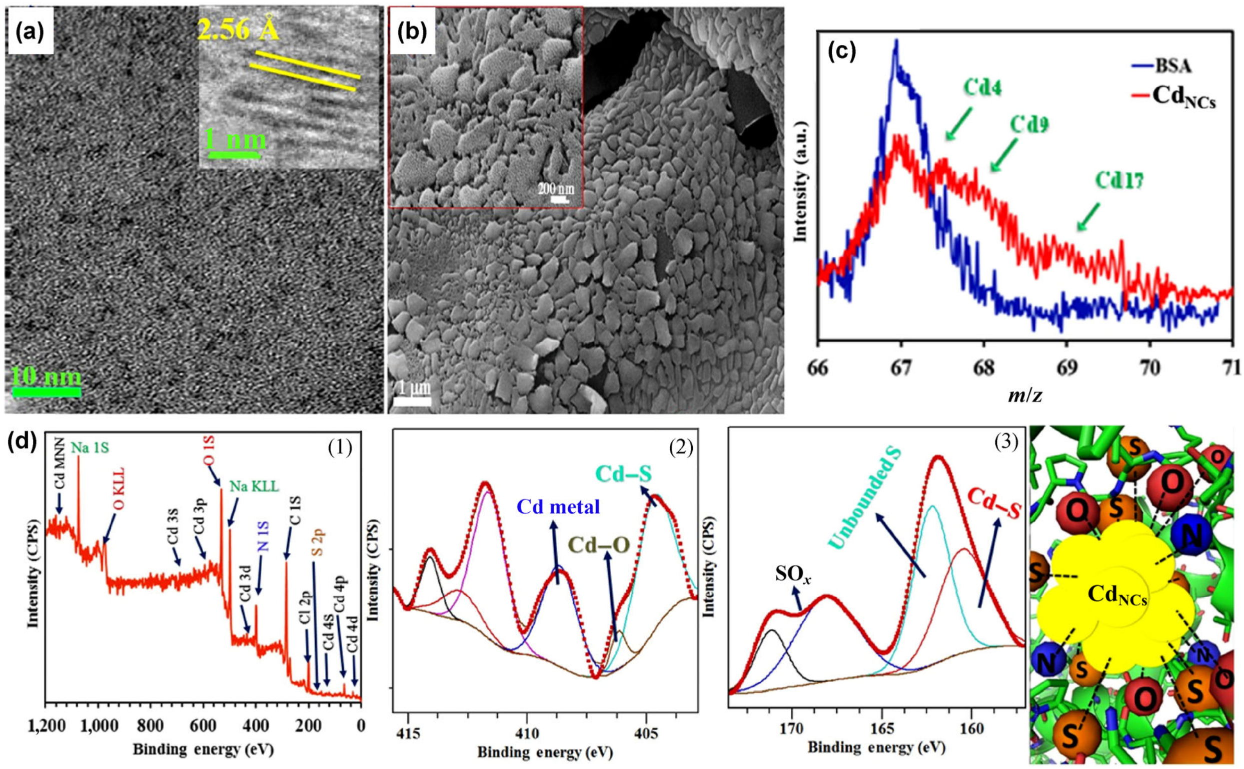

Figure 2 Characterization of Cd_{NCs}. (a) TEM image of Cd_{NCs} (inset: HR-TEM image of as-obtained Cd_{NCs} with a *d*-spacing of 2.56 Å, which closely matches the spacing (100) of the lattice planes of hexagonal Cd). (b) SEM images of Cd_{NCs} at two different magnifications. (c) MALDI-TOF MS spectra of pure BSA and Cd_{NCs} at pH 12, with assignment of the peaks to 4, 9, and 17 atoms as magic numbers of Cd in the Cd_{NCs}. (d) Wide-scan XPS spectra of Cd_{NCs}: (1) expanded XPS spectra of Cd showing two peaks, one around 405 eV ($3d_{5/2}$) and the other around 411 eV ($3d_{3/2}$), with deconvolution of each peak giving three distinct components that can be assigned to Cd^0, Cd–O, and Cd–S; (2) expanded XPS spectra of sulfur showing the binding energies of S $2p_{3/2}$, with the peaks at 161.9 and 168.9 eV attributed to sulfur bonded to Cd and oxidized sulfur, respectively; and (3) schematic representation of the functional groups involved in stabilization of the Cd_{NCs}.

to Cd–O (the oxygen can be attributed to hydroxyl and carboxyl groups of BSA residues) [70, 72], and the third band at a higher binding energy of 408.7 eV can be assigned to Cd^0. Similar deconvolution of the Cd $3d_{3/2}$ band yielded three distinct peaks with binding energies of 411.74, 412.42, and 414.3 eV, which can be assigned to Cd–S, Cd–O, and Cd^0, respectively. The presence of Cd^0 can be attributed to the BSA-assisted reduction of Cd ions during formation of Cd_{NCs}. The XPS spectrum of the S 2p region revealed binding energies of 161.4 and 169.2 eV (Fig. 2(d)(2)), which were attributed to sulfide (S^{2-}, probably in the form of CdS) and sulfur (in the form of metal sulfate), respectively. The peak at 161.4 eV could be divided into two peaks; the peak at the lower binding energy (160.5 eV) corresponds to Cd–S bonds, and the peak at the higher binding energy (162.3 eV) corresponds to unbonded sulfur [41, 70]. Because no external sulfur source was used, the XPS spectra reveal the explicit role of Cys residues in the synthesis of Cd_{NCs}. The deconvoluted unbonded sulfur band can be attributed to the 35 available Cys residues per BSA molecule, since perhaps not all of the Cys residues will participate in the stabilization process. Though less reactive, methionine (Met) (five per BSA molecule) is another source of sulfur that could also play a role in this process [73]. The deconvoluted peak at 169.2 eV was assigned to oxidized sulfur (Cd–SO_x, x = 2–4) [70, 74]. Oxidation of sulfur might be a consequence of protein degradation at the elevated pH of 12 during Cd_{NC} synthesis [41]. Furthermore, the N 1s spectrum of the sample shows a broad component with an unresolved fine structure positioned at 400.1 eV (N1 feature). This structure is expected because nitrogen atoms are involved in peptide bonds, amine groups in side chains, and indole (Trp) and imidazole (His) [75].

The presence of a peak at 396.5 eV may be attributed to Cd–N bonds (Fig. S12(a) in the ESM) [76]. In addition, the obtained O 1s XPS spectrum shows nonequivalent peaks, indicating that the carboxylate groups are bound unsymmetrically to the surface of Cd_{NCs} through their two oxygen atoms (Fig. S12(b) in the ESM). These results confirm the contribution of carboxyl and hydroxyl groups of BSA to the stabilization of NCs [11, 72]. Figure 2(d)(1) shows the proposed structure of NCs in the protein matrix.

The effective charge of the Cd_{NCs}, evaluated by ζ-potential measurement, plays an essential role in intermolecular interactions. The as-synthesized Cd_{NCs} had a ζ-potential of −32 mV, indicating an overall negative charge of the nanoplatform, which would induce great electrostatic repulsion among the particles. The fluorescence QY of the Cd_{NCs} was measured as 2.86% (λ_{ex} = 360 nm) with reference to quinine sulfate (54%) (Fig. S13 in the ESM). QYs of protein-templated M_{NCs} are generally lower than those of QDs, dendrimer-capped and polymer-coated NCs, and organic dyes. However, compared with other protein-templated NCs, BSA-templated Cd_{NCs} exhibit good QY, which makes them suitable for live-cell imaging applications. Our study showed that the change in the emission spectrum of synthesized Cd_{NCs} after 3 months of storage at room temperature is insignificant, confirming the high stability of Cd_{NCs} (Fig. S14(a) in the ESM). Moreover, the stability of Cd_{NCs} was investigated over a pH range of 4 to 12 (Fig. S14(b) in the ESM), and no significant change in the fluorescence intensity of the Cd_{NCs} was observed, even at an acidic pH of 4.5. These findings suggest that Cd_{NCs} could have great potential for cellular imaging and biosensing as well as drug delivery. However, for *in vivo* applications, the NCs should ideally have a small hydrodynamic diameter for efficient transmembrane permeation and urinary excretion, be able to target the desired tumor tissues while exhibiting prolonged circulation time and exquisite activity, and be able to selectively kill cancerous cells without affecting healthy cells. Cd_{NCs} seem to satisfy most of these requirements, since they can provide a multimodal delivery pathway. Cd_{NCs} deliver drugs to a specific tumor tissue through a combination of passive and active targeting along with stimulus-triggered release. The enhanced permeability and retention effect in tumor tissues, whereby the endothelial cells that line the walls of blood vessels become more permeable, plays a role in passive targeting. The mechanism behind active tumor targeting of Cd_{NCs} is the affinity of HA for CD44. The acidic environment of tumor tissues also triggers the release of the drug from the pH-sensitive Cd_{NCs}. However, the hydrodynamic size of NCs, measured by dynamic light scattering, is around 7.5 ± 0.5 nm (Fig. S15 in the ESM). Although Cd_{NCs} are smaller than gap junctions between endothelial cells in the tumor vasculature (100 to 600 nm), sinusoids in the spleen, and fenestrae of Kupffer cells in the liver (150 to 200 nm) [77], they do not undergo renal filtration (since the kidney filtration threshold is 5.5 nm) and the only excretion route is through the liver, via the bile [78–80].

3.2 Preparation and characterization of DOX-HA-Cd_{NCs}

For our drug delivery platform, we chose DOX as a model anticancer drug and used HA-conjugated Cd_{NCs} (HA-Cd_{NCs}) as a drug carrier, hydrophilic targeting moiety, and fluorescence probe. Preparation of the DOX-loaded nanocarrier (DOX-HA-Cd_{NCs}) is shown in Schemes 1(b) and 1(c), and the procedure is described in detail in the Experimental section of the ESM.

We attached HA, a large, linear, and hydrophilic macromolecule, to BSA to form a shell around the protein that would cover the antigenic determinants of BSA and increase the stability and solubility of the nanocarrier (Fig. S16 in the ESM shows the most important parts of HA, DOX, and Cd_{NCs} in the design of the nanoplatform). HA conjugated to BSA not only increased the circulation time of the nanocarrier, in a manner similar to that of polyethylene glycol, a gold-standard stabilizer in the field of drug delivery [81], but also served as a moiety for active targeted delivery of the anticancer drug [82]. Furthermore, HA limited the decrease in nanocarrier solubility induced by loading of DOX, a hydrophobic drug. We characterized the HA-Cd_{NCs} and DOX-HA-Cd_{NCs} using UV–vis absorption, FT-IR, and fluorescence spectroscopy, EDX, and SEM imaging.

Figure 3(a) shows UV–vis absorption spectra of Cd_{NCs}, HA, DOX, HA-Cd_{NCs}, and DOX-HA-Cd_{NCs}. The Cd_{NCs} show characteristic absorption bands at 285 and

350 nm, as previously discussed (Fig. 1(b)). HA has no obvious absorption band in the UV–vis region. Free DOX exhibits a strong and rather broad absorption peak at about 485 nm. As shown in Fig. 3, DOX-HA-Cd_{NCs} exhibit all of the characteristic peaks of the constituent components, demonstrating both the effective conjugation of HA to Cd_{NCs} and the successful loading of DOX onto the nanocarrier. The broadening of the DOX absorption maximum and its red shift to 515 nm can be ascribed to strong electrostatic and π–π stacking interactions in the DOX-HA-Cd_{NCs}.

The DOX-HA-Cd_{NC} preparation was analyzed by fluorescence spectroscopy. Under excitation at 360 nm, the Cd_{NCs} exhibited a peak at 485 nm. Conjugation of HA to the Cd_{NCs}, in appropriate ratios, just slightly quenched the emission of the NCs (Fig. S17 in the ESM), which renders them useful for bioimaging applications. Meanwhile, the fluorescence of the nanocarrier was dramatically quenched upon DOX loading (Fig. S18 in the ESM). The quenching of the DOX-HA-Cd_{NC} fluorescence can be ascribed to the energy transfer between DOX and the nanocarrier, which also confirms successful loading of DOX onto the nanocarrier. It should be noted that the quenching of the fluorescence of the nanocarrier upon DOX loading and its reappearance with DOX unloading serve as an indicator of whether the nanocarrier has unloaded its cargo.

We also recorded the FT-IR spectra of the DOX-HA-Cd_{NCs} and their individual components to further confirm the successful formation of HA-Cd_{NCs} and DOX-HA-Cd_{NCs}. Figure 3(b) shows the characteristic peaks of Cd_{NCs} (curve (1)), HA (curve (2)), and DOX (curve (3)), which are also assigned in more detail in Table S1 in the ESM [60, 83].

The spectrum of HA shows several sharp bands corresponding to C–O–C stretching of ether groups (1,045 cm^{-1}), symmetric carboxylate stretching (1,408 cm^{-1}), a skeletal acetal band (1,149 cm^{-1}), C–O stretching (1,047 cm^{-1}), amide I groups (1,619 cm^{-1}), C–H stretching (2,916 cm^{-1}), and O–H stretching (3,394 cm^{-1}). The Cd_{NCs} bands are an amide II band at 1,535 cm^{-1}, an

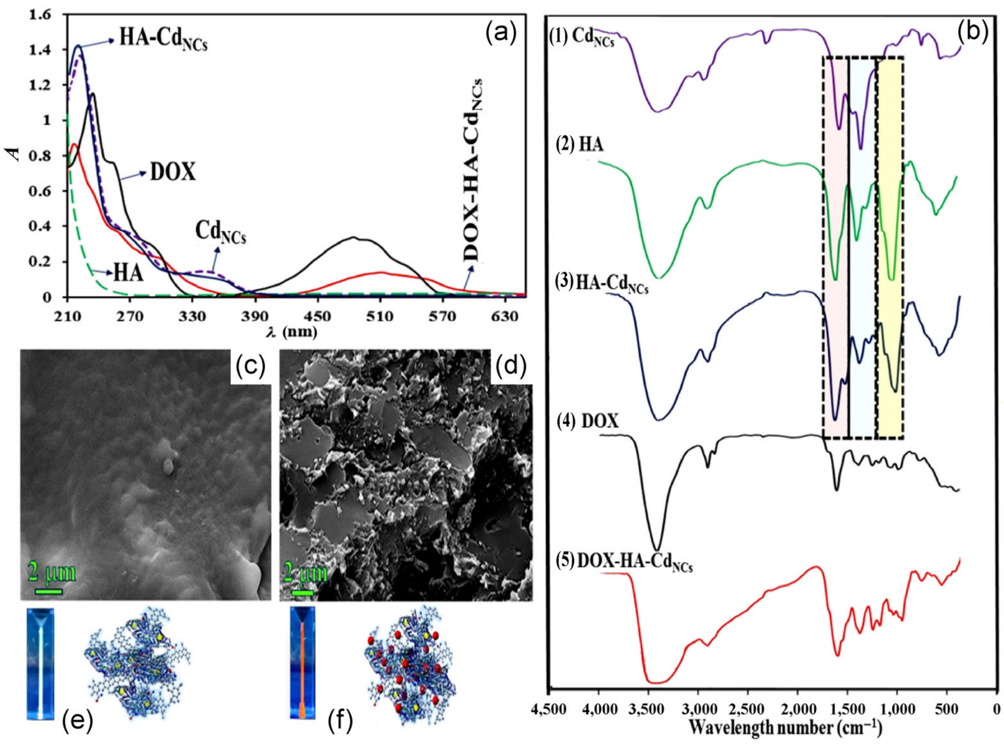

Figure 3 Characterization of HA-Cd_{NCs} and DOX-HA-Cd_{NCs}. (a) UV–vis absorption spectra of Cd_{NCs}, HA, HA-Cd_{NCs}, DOX, and DOX-HA-Cd_{NCs}. (b) FT-IR spectra of Cd_{NCs} (1), HA (2), HA-Cd_{NCs} (3), DOX (4), and DOX-HA-Cd_{NCs} (5). (c) and (d) SEM images of HA-Cd_{NCs} and DOX-HA-Cd_{NCs}, respectively. (e) and (f) Photographs under UV light and schematic representations of HA-Cd_{NCs} and DOX-HA-Cd_{NCs}, respectively.

amide I band at 1,657 cm^{-1}, a C–H stretching band at 2,930 cm^{-1}, and an O–H stretching band at 3,315 cm^{-1}. The corresponding bands of HA-Cd_{NCs} in the same regions have the features of both pure HA and Cd_{NCs}, confirming the conjugation of HA to Cd_{NCs}. However, the shift in the amide II band position indicates that the amide II group is an interaction site for conjugation of HA to Cd_{NCs}. In addition, the change in distance between the amide I and amide II peaks in the HA-Cd_{NCs} spectrum compared with the Cd_{NCs} spectrum confirms the creation of new amide bonds in the HA-Cd_{NCs}. The change in the COOH band in the HA-Cd_{NCs} spectrum also demonstrates a hydrogen-bonding interaction between HA and Cd_{NCs}. The FT-IR spectrum of DOX shows several bands in the investigated region, details of which are presented in Table S1 (in the ESM). In contrast to the FT-IR spectra of HA-Cd_{NCs} and free DOX, the spectrum of DOX-HA-Cd_{NCs} shows new bands at 815 and 1,116 cm^{-1} corresponding to C–O–CH_3 stretching vibrations. Additionally, the shift in the NH_2 wagging band from 794 to 797 cm^{-1} confirms intermolecular hydrogen bonding between DOX and the nanocarrier [84].

We also traced the changes in the morphology of the Cd_{NCs} after HA conjugation and DOX loading with FE-SEM imaging. The FE-SEM image of HA-Cd_{NCs} shows that the HA provides a cover for Cd_{NCs}, which increases the biocompatibility of the nanocarrier. The change in morphology of the DOX-loaded nanocarrier can be attributed to a strong interaction between DOX and the nanocarrier (Fig. 3(d)). Furthermore, the EDX spectrum confirmed the presence of Cd in HA-Cd_{NCs} and DOX-HA-Cd_{NCs} (Figs. S19 and S20 in the ESM). The density of HA strongly influences the performance of Cd_{NCs}. HA increases the binding of the nanocarrier to cells and significantly improves cell viability, but excess HA quenches the fluorescence of the Cd_{NCs} (Fig. S21 in the ESM). An HA density of 1.25 mg HA/mg Cd_{NCs} was chosen as the optimum trade-off between biocompatibility and fluorescence intensity. We also used different DOX:HA-Cd_{NCs} weight ratios to obtain the best DOX loading efficiency (DLEDOX) and DOX encapsulation efficiency (EEDOX) (Fig. S22 in the ESM). At a DOX:HA-Cd_{NCs} weight ratio of 3:2, the values of DLEDOX and EEDOX were 48.7% and 75.6%, respectively. These values are higher than those reported previously for other drug carriers, including polymer nanoparticles, metal nanoparticles, and graphene-based nanocarriers [82, 85, 86].

3.3 *In vitro* drug release from DOX-HA-Cd_{NCs}

In this study, a pH-responsive drug delivery vehicle was fabricated for controlled and targeted DOX delivery. We studied the release of DOX from DOX-HA-Cd_{NCs} at different pH values (Fig. 4). Particle size, pH, carrier materials, and the nature of the drug–nanocarrier interactions are some of the important factors influencing the drug release profile. DOX release from the nanocarriers was investigated in buffers of different pH, one at pH 5.3, similar to the environment of a tumor cell, and the other at pH 7.4, i.e., normal physiological pH. As shown in Figs. 4(a) and 4(b), DOX-HA-Cd_{NCs} exhibited high stability at pH 7.4 and released less than 26% of DOX in 24 h, while 74% of DOX was released at pH 5.3 during the same period, indicating that an acidic medium facilitates the release of DOX. The release of DOX can be mainly attributed to the increase in hydrophilicity and water solubility of DOX in an acidic environment. In addition, the electrostatic interaction between the nanocarrier and DOX decreases as a consequence of the decrease in the negative charge of the Cd_{NCs} in an acidic medium. This feature of the as-designed nanocarrier is highly desirable and beneficial for targeted cancer therapy because the pH of most tumors is about one order of magnitude lower than that of normal tissue. Furthermore, given the strong hydrogen-bonding, hydrophobic, and electrostatic interactions between DOX and HA-Cd_{NCs}, the release of DOX from DOX-HA-Cd_{NCs} was slower than the release of free DOX at pH 5.3 and pH 7.4. Therefore, the pH-responsive behavior of DOX-HA-Cd_{NCs} is promising for targeting the acidic environments of tumor cells and intracellular compartments such as endosomes and lysosomes, thus enhancing cytotoxicity to cancer cells while decreasing drug toxicity to plasma and normal tissue.

3.4 *In vitro* bioimaging and cellular uptake

To visualize the cellular uptake of Cd_{NCs} and HA-Cd_{NCs} and to evaluate the targeted drug delivery performance of the nanoplatform, we applied the nanocarriers to MCF-7 human breast cancer cells, which overexpress

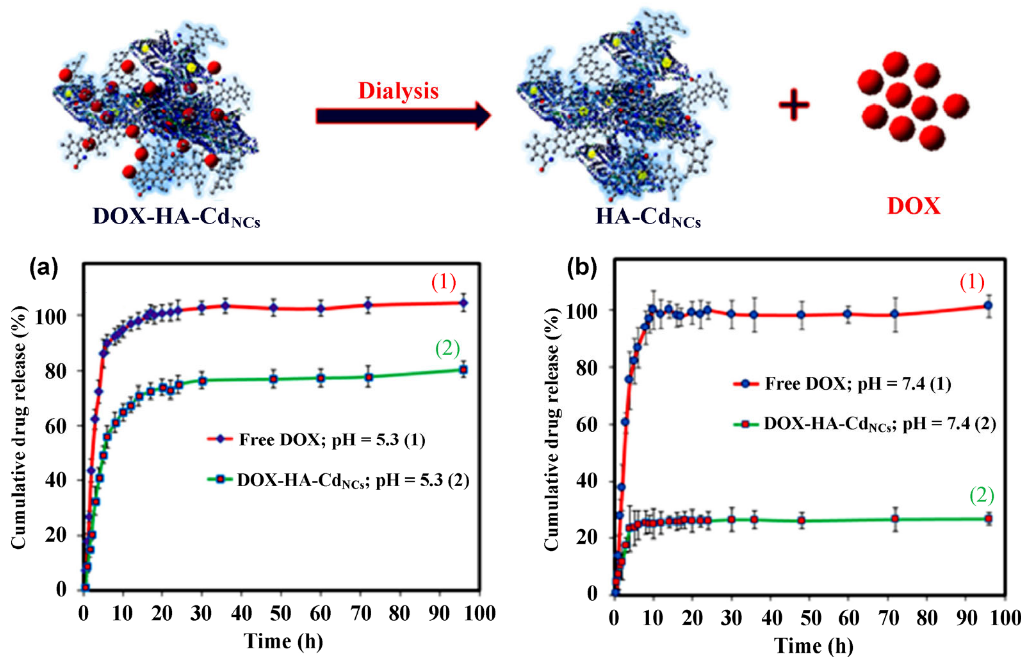

Figure 4 Release profiles of DOX under physiological and acidic conditions, determined by UV–vis absorption spectroscopy. (a) Release profiles of free DOX (1) and DOX-HA-Cd$_{NCs}$ (2) at an acidic pH (5.3) similar to that found in the tumor environment. (b) Release profiles of free DOX (1) and DOX-HA-Cd$_{NCs}$ (2) at physiological pH (7.4).

CD44 as a surface HA receptor, and HEK293 cells, which have no HA receptor on their surface. We incubated the MCF-7 cells separately with HA-Cd$_{NCs}$ and Cd$_{NCs}$. As shown in Fig. 5, MCF-7 cells incubated with HA-Cd$_{NCs}$ showed much stronger blue-green fluorescence than cells incubated with Cd$_{NCs}$, demonstrating HA receptor-mediated endocytosis of HA-Cd$_{NCs}$, but not Cd$_{NCs}$, into MCF-7 breast cancer cells. As expected, no fluorescence was observed in the control experiment without a nanocarrier. Figure 5 also shows an insignificant change in the fluorescence intensity of HEK293 cells after incubation with Cd$_{NCs}$ and HA-Cd$_{NCs}$. These results demonstrate that the uptake of HA-Cd$_{NCs}$ by an HA receptor-positive cell line (MCF-7) is considerably greater than that by an HA receptor-negative cell line (HEK293). The enhanced permeability and retention effect might also play a vital role in the accumulation of more HA-Cd$_{NCs}$ in cancer cells.

We also used HeLa cells, which overexpress HA receptors, to study the potential application of the nanocarrier as a contrast agent for *in vitro* bioimaging. The fabricated nanocarrier system exhibited a high-resolution bioimaging capability (Fig. S23 in the ESM). The cellular uptake of DOX was investigated by fluorescence microscopy after incubation of MCF-7 cells with free DOX or DOX-HA-Cd$_{NCs}$ for 6 h. As shown in Fig. 5, the fluorescence intensity was much stronger in MCF-7 cells treated with DOX-HA-Cd$_{NCs}$ than in cells treated with free DOX (at the same concentration), indicating that CD44 receptor-mediated endocytosis facilitates the cellular uptake of DOX. In contrast, HEK293 cells showed very weak fluorescence after incubation with DOX-HA-Cd$_{NCs}$, even lower than that observed after incubation with free DOX. Thus, selective uptake of the drug by target cells provides the basis for targeted cancer therapy with HA-CdNCs. We also demonstrated dose-dependent cellular uptake and release of DOX in MCF-7 cells (Fig. 6). At a low concentration of free DOX or DOX-HA-Cd$_{NCs}$ (0.5 μg/mL), the fluorescence intensity was much stronger in MCF-7 cells incubated with DOX-HA-Cd$_{NCs}$ than in cells incubated with free DOX, while the fluorescence intensity was nearly the same in MCF-7 cells incubated with a high concentration of free DOX or DOX-HA-Cd$_{NCs}$ (5 μg/mL). These data

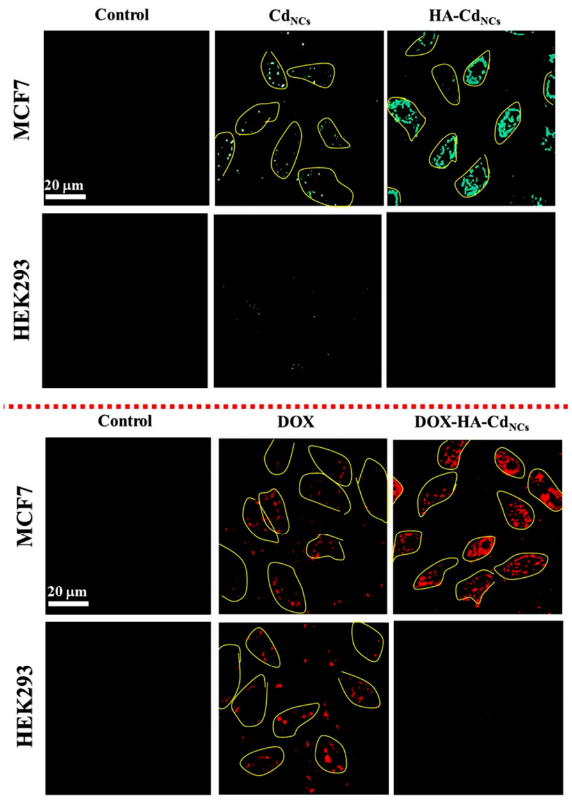

Figure 5 *In vitro* imaging of cellular uptake of nanocarriers. Fluorescence microscopy images of $CD44^+$ MCF-7 cells (upper series) and $CD44^-$ HEK293 cells (bottom series) incubated for 6 h with Cd_{NCs}, HA-Cd_{NCs}, DOX, and DOX-HA-Cd_{NCs}. The first image in each series corresponds to untreated cells. To deliver the correct wavelength of light and collect as much signal as possible, we used a 4′,6-diamidino-2-phenylindole filter with an excitation wavelength of 352 to 402 nm and an emission wavelength of 417 to 477 nm (upper panel of the figure, corresponding to cellular imaging, i.e., HA-Cd_{NC} emission) and a fluorescein isothiocyanate filter with an excitation wavelength of 478 to 495 nm and an emission wavelength of 505 to 570 nm (bottom panel of the figure, corresponding to drug delivery, i.e., DOX emission).

confirm the selective receptor-mediated uptake of DOX-HA-Cd_{NCs} by MCF-7 cells. However, high doses of DOX should not be used because the fluorescence intensity of cells before and after drug uptake can be better differentiated with a low-dose regimen of DOX. Furthermore, a high-dose drug regimen has severe side effects, such as toxicity, which can limit the efficacy of DOX toward tumor cells. The fluorescence images shown in Figs. 5 and 6 strongly suggest specific uptake of DOX-HA-Cd_{NCs} by cells overexpressing CD44, presumably through HA receptor-mediated endocytosis. They also suggest that DOX-HA-Cd_{NCs} can effectively deliver DOX to target MCF-7 tumor

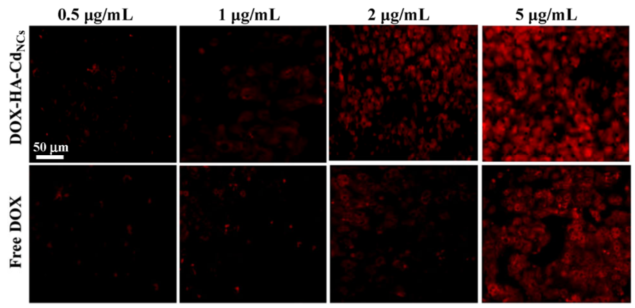

Figure 6 Fluorescence microscopy images of $CD44^+$ MCF-7 cells treated for 6 h with DOX-HA-Cd_{NCs} (upper series) and free DOX (bottom series) at DOX concentrations of 0.5, 1.0, 2.0, and 5.0 μg/mL (left to right, respectively).

cells. These results confirm that the designed nanocarrier can be used as an intracellular drug delivery system and for cellular-level monitoring of therapeutic efficiency. Its application in an *in vivo* model will be examined in the near future.

3.5 Cytotoxicity

We next explored the effect of Cd_{NCs} and HA-Cd_{NCs} on the viability of MCF-7 and HEK293 cells and observed significant cell survival, i.e., low cytotoxicity of Cd_{NCs} and HA-Cd_{NCs}. These results confirm that Cd_{NCs} have high biocompatibility even at a relatively high concentration of 1 mg/mL (Fig. 7). Only at higher concentrations (>2 mg/mL) do the NCs show slight cytotoxicity to cells. Furthermore, the toxicity of the NCs is reduced when HA is conjugated to the Cd_{NCs} surface, because of the high biocompatibility of HA [59]. The slight toxicity of Cd_{NCs} and HA-Cd_{NCs} to HEK293 cells originates from the slower growth rate of HEK293 cells compared with MCF-7 cells [43].

Finally, we investigated the inhibitory effect of DOX released from DOX-HA-Cd_{NCs} on the growth of MCF-7 breast cancer cells. In a control experiment, the cytotoxicity of free DOX was also investigated. The results indicate that DOX-HA-Cd_{NCs} are much more cytotoxic to MCF-7 cells than free DOX. In contrast, the cytotoxicity of DOX-HA-Cd_{NCs} to HEK293 cells was lower than that of free DOX, indicating that DOX-HA-Cd_{NCs} are less toxic to normal cells. Nanocarrier-assisted targeted drug delivery with pH-responsive yet sustained drug release guarantees the superiority of the proposed drug delivery approach over other

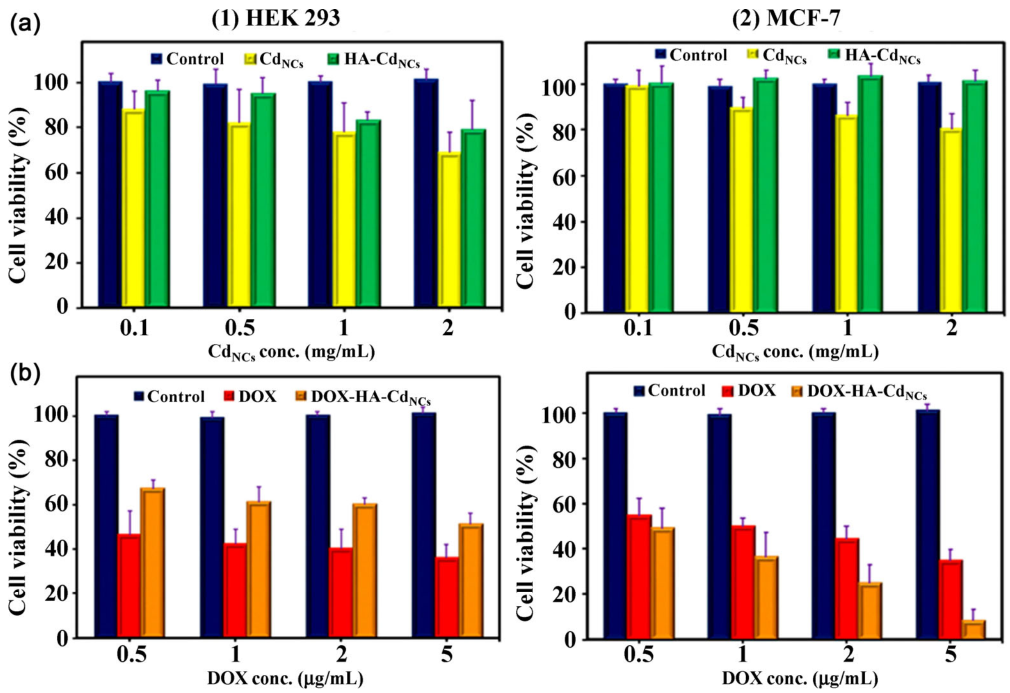

Figure 7 *In vitro* cytotoxicity determined by the MTT assay. (a) Relative viability of (1) HEK293 cells (control cells) and (2) $CD44^+$ MCF-7 cells (target cells) after treatment with Cd_{NCs} and HA-Cd_{NCs}. (b) Cytotoxicity of free DOX and DOX-HA-Cd_{NCs} at different concentrations after treatment of cells for 24 h.

methods. These results suggest that the DOX-HA-Cd_{NCs} drug delivery system is promising for targeted cancer therapy, since the proposed system achieves the same cytotoxicity to tumor cells at a lower dose of DOX, thereby reducing negative effects on normal cells.

4 Conclusions

In summary, we have developed a green-chemistry route for the preparation of a potent nanoplatform consisting of bright-blue emitting Cd_{NCs} as an effective delivery vehicle and bioimaging probe, HA as a targeting ligand, and DOX as a model anticancer drug. The nanoplatform exhibits strong and efficient therapeutic activity and sustained pH-sensitive DOX release that differs from that of free DOX. The efficient tumor targeting ability and superior cellular uptake can be mainly attributed to the HA shell, since receptors for HA are overexpressed on many cancer cells. The NCs have a small hydrodynamic diameter, resulting in a nanoplatform with renal clearance and a prolonged circulation time. Covalent, hydrophobic, and electrostatic interactions of DOX with the nanoplatform diminish the initial burst release of DOX and dramatically enhance therapeutic efficacy. Overall, the nanoplatform developed in this study shows great promise for simultaneous receptor-mediated tumor targeting, cancer chemotherapy, and bioimaging.

Acknowledgements

Financial support of this work by the Tarbiat Modares University Research Council is gratefully acknowledged.

Electronic Supplementary Material: Supplementary material (detailed description on procedures, and further characterizations, including synthesis, optimization, and characterization of Cd_{NCs}, HA-Cd_{NCs}, and DOX-HA-Cd_{NCs}; calculating quantum yield; a Jellium model for assigning the most valid number of the atoms in the NCs; drug loading and release; cellular uptake and cytotoxicity) is available in the online version of this article at http://dx.doi.org/10.1007/s12274-016-1201-z.

References

[1] Pelaz, B.; Jaber, S.; de Aberasturi, D. J.; Wulf, V.; Aida, T.; de la Fuente, J. M.; Feldmann, J.; Gaub, H. E.; Josephson, L.; Kagan, C. R. et al. The state of nanoparticle-based nanoscience and biotechnology: Progress, promises, and challenges. *ACS Nano* **2012**, *6*, 8468–8483.

[2] Ye, E. Y.; Regulacio, M. D.; Zhang, S. Y.; Loh, X. J.; Han, M. Y. Anisotropically branched metal nanostructures. *Chem. Soc. Rev.* **2015**, *44*, 6001–6017.

[3] Pendashteh, A.; Mousavi, M. F.; Rahmanifar, M. S. Fabrication of anchored copper oxide nanoparticles on graphene oxide nanosheets via an electrostatic coprecipitation and its application as supercapacitor. *Electrochim. Acta* **2013**, *88*, 347–357.

[4] Kumar, A.; Kumar, V. Biotemplated inorganic nanostructures: Supramolecular directed nanosystems of semiconductor(s)/metal(s) mediated by nucleic acids and their properties. *Chem. Rev.* **2014**, *114*, 7044–7078.

[5] Mehdinla, A.; Mousavi, M. F. Enhancing extraction rate in solid-phase microextraction by using nano-structured polyaniline coating. *J. Sep. Sci.* **2008**, *31*, 3565–3572.

[6] Ghanbari, K.; Bathaie, S. Z.; Mousavi, M. F. Electrochemically fabricated polypyrrole nanofiber-modified electrode as a new electrochemical DNA biosensor. *Biosens. Bioelectron.* **2008**, *23*, 1825–1831.

[7] Yousef Elahi, M.; Bathaie, S. Z.; Kazemi, S. H.; Mousavi, M. F. DNA immobilization on a polypyrrole nanofiber modified electrode and its interaction with salicylic acid/aspirin. *Anal. Biochem.* **2011**, *411*, 176–184.

[8] Yousef Elahi, M.; Bathaie, S. Z.; Mousavi, M. F.; Hoshyar, R.; Ghasemi, S. A new DNA-nanobiosensor based on G-quadruplex immobilized on carbon nanotubes modified glassy carbon electrode. *Electrochim. Acta* **2012**, *82*, 143–151.

[9] Ilkhani, H.; Sarparast, M.; Noori, A.; Bathaie, S. Z.; Mousavi, M. F. Electrochemical aptamer/antibody based sandwich immunosensor for the detection of EGFR, a cancer biomarker, using gold nanoparticles as a signaling probe. *Biosens. Bioelectron.* **2015**, *74*, 491–497.

[10] Moradi, N.; Mousavi, M. F.; Mehrgardi, M. A.; Noori, A. Preparation of a new electrochemical biosensor for single base mismatch detection in DNA. *Anal. Methods* **2013**, *5*, 6531–6538.

[11] Wu, N. Q.; Fu, L.; Su, M.; Aslam, M.; Wong, K. C.; Dravid, V. P. Interaction of fatty acid monolayers with cobalt nanoparticles. *Nano Lett.* **2004**, *4*, 383–386.

[12] Bagheryan, Z.; Noori, A.; Bathaie, S. Z.; Yousef-Elahi, M.; Mousavi, M. F. Preparation of a new nanobiosensor for the determination of some biogenic polyamines and investigation of their interaction with DNA. *Biosens. Bioelectron.* **2016**, *77*, 767–773.

[13] Xue, T.; Peng, B.; Xue, M.; Zhong, X.; Chiu, C. Y.; Yang, S.; Qu, Y. Q.; Ruan, L. Y.; Jiang, S.; Dubin, S. et al. Integration of molecular and enzymatic catalysts on graphene for biomimetic generation of antithrombotic species. *Nat. Commun.* **2014**, *5*, 3200.

[14] Song, H. Metal hybrid nanoparticles for catalytic organic and photochemical transformations. *Acc. Chem. Res.* **2015**, *48*, 491–499.

[15] Bao, G.; Mitragotri, S.; Tong, S. Multifunctional nanoparticles for drug delivery and molecular imaging. *Annu. Rev. Biomed. Eng.* **2013**, *15*, 253–282.

[16] Doane, T. L.; Burda, C. The unique role of nanoparticles in nanomedicine: Imaging, drug delivery and therapy. *Chem. Soc. Rev.* **2012**, *41*, 2885–2911.

[17] Hong, A. J.; Song, E. B.; Yu, H. S.; Allen, M. J.; Kim, J.; Fowler, J. D.; Wassei, J. K.; Park, Y.; Wang, Y.; Zou, J. et al. Graphene flash memory. *ACS Nano* **2011**, *5*, 7812–7817.

[18] Olivieri, A.; Chen, C. K.; Hassan, S.; Lisicka-Skrzek, E.; Tait, R. N.; Berini, P. Plasmonic nanostructured metal-oxide-semiconductor reflection modulators. *Nano Lett.* **2015**, *15*, 2304–2311.

[19] Shao, Y. L.; El-Kady, M. F.; Wang, L. J.; Zhang, Q. H.; Li, Y. G.; Wang, H. Z.; Mousavi, M. F.; Kaner, R. B. Graphene-based materials for flexible supercapacitors. *Chem. Soc. Rev.* **2015**, *44*, 3639–3665.

[20] Lu, Y. Z.; Chen, W. Sub-nanometre sized metal clusters: From synthetic challenges to the unique property discoveries. *Chem. Soc. Rev.* **2012**, *41*, 3594–3623.

[21] Wen, X. M.; Yu, P.; Toh, Y.-R.; Tang, J. Quantum confined stark effect in Au_8 and Au_{25} nanoclusters. *J. Phys. Chem. C* **2013**, *117*, 3621–3626.

[22] Ghosh, R.; Sahoo, A. K.; Ghosh, S. S.; Paul, A.; Chattopadhyay, A. Blue-emitting copper nanoclusters synthesized in the presence of lysozyme as candidates for cell labeling. *ACS Appl. Mater. Interfaces* **2014**, *6*, 3822–3828.

[23] Mathew, A.; Pradeep, T. Noble metal clusters: Applications in energy, environment, and biology. *Part. Part. Syst. Charact.* **2014**, *31*, 1017–1053.

[24] Molaabasi, F.; Hosseinkhani, S.; Moosavi-Movahedi, A. A.; Shamsipur, M. Hydrogen peroxide sensitive hemoglobin-capped gold nanoclusters as a fluorescence enhancing sensor for the label-free detection of glucose. *RSC Adv.* **2015**, *5*, 33123–33135.

[25] Tiwari, J. N.; Nath, K.; Kumar, S.; Tiwari, R. N.; Kemp, K. C.; Le, N. H.; Youn, D. H.; Lee, J. S.; Kim, K. S. Stable platinum nanoclusters on genomic DNA-graphene oxide with a high oxygen reduction reaction activity. *Nat. Commun.* **2013**, *4*, 2221.

[26] Qin, W.; Lohrman, J.; Ren, S. Q. Magnetic and optoelectronic properties of gold nanocluster-thiophene assembly. *Angew*

Chem., Int. Ed. **2014**, *53*, 7316–7319.
[27] Khandelia, R.; Bhandari, S.; Pan, U. N.; Ghosh, S. S.; Chattopadhyay, A. Gold nanocluster embedded albumin nanoparticles for two-photon imaging of cancer cells accompanying drug delivery. *Small* **2015**, *11*, 4075–4081.
[28] Jin, R. C. Atomically precise metal nanoclusters: Stable sizes and optical properties. *Nanoscale* **2015**, *7*, 1549–1565.
[29] Wu, Z. K.; Jin, R. C. On the ligand's role in the fluorescence of gold nanoclusters. *Nano Lett.* **2010**, *10*, 2568–2573.
[30] Wan, X. K.; Lin, Z. W.; Wang, Q. M. Au_{20} nanocluster protected by hemilabile phosphines. *J. Am. Chem. Soc.* **2012**, *134*, 14750–14752.
[31] Tanaka, S. I.; Miyazaki, J.; Tiwari, D. K.; Jin, T.; Inouye, Y. Fluorescent platinum nanoclusters: Synthesis, purification, characterization, and application to bioimaging. *Angew Chem., Int. Ed.* **2011**, *50*, 431–435.
[32] Zhang, Y.; Zhu, C. F.; Zhang, L.; Tan, C. L.; Yang, J.; Chen, B.; Wang, L. H.; Zhang, H. DNA-templated silver nanoclusters for multiplexed fluorescent DNA detection. *Small* **2015**, *11*, 1385–1389.
[33] Jia, X. F.; Li, J.; Han, L.; Ren, J. T.; Yang, X.; Wang, E. K. DNA-hosted copper nanoclusters for fluorescent identification of single nucleotide polymorphisms. *ACS Nano* **2012**, *6*, 3311–3317.
[34] Cui, Y. Y.; Wang, Y. L.; Liu, R. L.; Sun, Z. P.; Wei, Y. T.; Zhao, Y. L.; Gao, X. Y. Serial silver clusters biomineralized by one peptide. *ACS Nano* **2011**, *5*, 8684–8689.
[35] Song, W.; Liang, R. P.; Wang, Y.; Zhang, L.; Qiu, J. D. Green synthesis of peptide-templated gold nanoclusters as novel fluorescence probes for detecting protein kinase activity. *Chem. Commun.* **2015**, *51*, 10006–10009.
[36] Chen, H.; Lin, L.; Li, H. F.; Li, J. Z.; Lin, J. M. Aggregation-induced structure transition of protein-stabilized zinc/copper nanoclusters for amplified chemiluminescence. *ACS Nano* **2015**, *9*, 2173–2183.
[37] Wang, Y. L.; Chen, J. J.; Irudayaraj, J. Nuclear targeting dynamics of gold nanoclusters for enhanced therapy of $HER2^+$ breast cancer. *ACS Nano* **2011**, *5*, 9718–9725.
[38] Goswami, N.; Zheng, K. Y.; Xie, J. P. Bio-NCs—The marriage of ultrasmall metal nanoclusters with biomolecules. *Nanoscale* **2014**, *6*, 13328–13347.
[39] Xu, Y. L.; Sherwood, J.; Qin, Y.; Crowley, D.; Bonizzoni, M.; Bao, Y. P. The role of protein characteristics in the formation and fluorescence of Au nanoclusters. *Nanoscale* **2014**, *6*, 1515–1524.
[40] Goswami, N.; Baksi, A.; Giri, A.; Xavier, P. L.; Basu, G.; Pradeep, T.; Pal, S. K. Luminescent iron clusters in solution. *Nanoscale* **2014**, *6*, 1848–1854.
[41] Le Guével, X.; Hötzer, B.; Jung, G.; Hollemeyer, K.; Trouillet, V.; Schneider, M. Formation of fluorescent metal (Au, Ag) nanoclusters capped in bovine serum albumin followed by fluorescence and spectroscopy. *J. Phys. Chem. C* **2011**, *115*, 10955–10963.
[42] Chen, Y. N.; Chen, P. C.; Wang, C. W.; Lin, Y. S.; Ou, C. M.; Ho, L. C.; Chang, H. T. One-pot synthesis of fluorescent BSA-Ce/Au nanoclusters as ratiometric pH probes. *Chem. Commun.* **2014**, *50*, 8571–8574.
[43] Dong, L. Y.; Li, M. L.; Zhang, S.; Li, J.; Shen, G. X.; Tu, Y. T.; Zhu, J. T.; Tao, J. Cytotoxicity of BSA-stabilized gold nanoclusters: *In vitro* and *in vivo* study. *Small* **2015**, *11*, 2571–2581.
[44] Ghosh, S.; Das, N. K.; Anand, U.; Mukherjee, S. Photostable copper nanoclusters: Compatible Förster resonance energy-transfer assays and a nanothermometer. *J. Phys. Chem. Lett.* **2015**, *6*, 1293–1298.
[45] Abbaspour, A.; Noori, A. Electrochemical detection of individual single nucleotide polymorphisms using monobase-modified apoferritin-encapsulated nanoparticles. *Biosens. Bioelectron.* **2012**, *37*, 11–18.
[46] Chen, T.; Xu, S.; Zhao, T.; Zhu, L.; Wei, D. F.; Li, Y. Y.; Zhang, H. X.; Zhao, C. Y. Gold nanocluster-conjugated amphiphilic block copolymer for tumor-targeted drug delivery. *ACS Appl. Mater. Interfaces* **2012**, *4*, 5766–5774.
[47] Zhang, P.; Yang, X. X.; Wang, Y.; Zhao, N. W.; Xiong, Z. H.; Huang, C. Z. Rapid synthesis of highly luminescent and stable Au_{20} nanoclusters for active tumor-targeted imaging *in vitro* and *in vivo*. *Nanoscale* **2014**, *6*, 2261–2269.
[48] Weng, J. F.; Ren, J. C. Luminescent quantum dots: A very attractive and promising tool in biomedicine. *Curr. Med. Chem.* **2006**, *13*, 897–909.
[49] Das, T.; Ghosh, P.; Shanavas, M. S.; Maity, A.; Mondal, S.; Purkayastha, P. Protein-templated gold nanoclusters: Size dependent inversion of fluorescence emission in the presence of molecular oxygen. *Nanoscale* **2012**, *4*, 6018–6024.
[50] Zhou, W. J.; Cao, Y. Q.; Sui, D. D.; Guan, W. J.; Lu, C.; Xie, J. P. Ultrastable BSA-capped gold nanoclusters with a polymer-like shielding layer against reactive oxygen species in living cells. *Nanoscale* **2016**, *8*, 9614–9620.
[51] Chou, L. Y. T.; Chan, W. C. W. Nanotoxicology: No signs of illness. *Nat. Nanotechnol.* **2012**, *7*, 416–417.
[52] Xia, X. D.; Zhang, Y.; Wang, J. X. Novel fabrication of highly fluorescent Pt nanoclusters and their applications in hypochlorite assay. *RSC Adv.* **2014**, *4*, 25365–25368.
[53] Ji, J. W.; Wang, G.; Wang, T. W.; You, X. Z.; Xu, X. X. Thiolate-protected Ni_{39} and Ni_{41} nanoclusters: Synthesis, self-assembly and magnetic properties. *Nanoscale* **2014**, *6*, 9185–9191.

[54] Goswami, N.; Giri, A.; Bootharaju, M. S.; Xavier, P. L.; Pradeep, T.; Pal, S. K. Copper quantum clusters in protein matrix: Potential sensor of Pb^{2+} ion. *Anal. Chem.* **2011**, *83*, 9676–9680.

[55] Ghosh, S. C.; Neslihan Alpay, S.; Klostergaard, J. CD44: A validated target for improved delivery of cancer therapeutics. *Expert Opin. Ther. Targets* **2012**, *16*, 635–650.

[56] Zhang, L. W.; Gao, S.; Zhang, F.; Yang, K.; Ma, Q. J.; Zhu, L. Activatable hyaluronic acid nanoparticle as a theranostic agent for optical/photoacoustic image-guided photothermal therapy. *ACS Nano* **2014**, *8*, 12250–12258.

[57] Wei, X.; Senanayake, T. H.; Warren, G.; Vinogradov, S. V. Hyaluronic acid-based nanogel-drug conjugates with enhanced anticancer activity designed for the targeting of CD44-positive and drug-resistant tumors. *Bioconjug. Chem.* **2013**, *24*, 658–668.

[58] Kim, K. S.; Hur, W.; Park, S. J.; Hong, S. W.; Choi, J. E.; Goh, E. J.; Yoon, S. K.; Hahn, S. K. Bioimaging for targeted delivery of hyaluronic Acid derivatives to the livers in cirrhotic mice using quantum dots. *ACS Nano* **2010**, *4*, 3005–3014.

[59] Abdullah-Al-Nahain; Lee, J.-E.; In, I.; Lee, H.; Lee, K. D.; Jeong, J. H.; Park, S. Y. Target delivery and cell imaging using hyaluronic acid-functionalized graphene quantum dots. *Mol. Pharm.* **2013**, *10*, 3736–3744.

[60] Lim, E.-K.; Kim, H.-O.; Jang, E.; Park, J.; Lee, K.; Suh, J.-S.; Huh, Y.-M.; Haam, S. Hyaluronan-modified magnetic nanoclusters for detection of CD44-overexpressing breast cancer by MR imaging. *Biomaterials* **2011**, *32*, 7941–7950.

[61] Lee, T.; Lim, E.-K.; Lee, J.; Kang, B.; Choi, J.; Park, H. S.; Suh, J.-S.; Huh, Y.-M.; Haam, S. Efficient CD44-targeted magnetic resonance imaging (MRI) of breast cancer cells using hyaluronic acid (HA)-modified $MnFe_2O_4$ nanocrystals. *Nanoscale Res. Lett.* **2013**, *8*, 149.

[62] Walter, M.; Akola, J.; Lopez-Acevedo, O.; Jadzinsky, P. D.; Calero, G.; Ackerson, C. J.; Whetten, R. L.; Grönbeck, H.; Häkkinen, H. A unified view of ligand-protected gold clusters as superatom complexes. *Proc. Natl. Acad. Sci. USA* **2008**, *105*, 9157–9162.

[63] Greenfield, N. J. Using circular dichroism spectra to estimate protein secondary structure. *Nat. Protoc.* **2006**, *1*, 2876–2890.

[64] Baksi, A.; Xavier, P. L.; Chaudhari, K.; Goswami, N.; Pal, S. K.; Pradeep, T. Protein-encapsulated gold cluster aggregates: The case of lysozyme. *Nanoscale* **2013**, *5*, 2009–2016.

[65] Xie, J. P.; Zheng, Y. G.; Ying, J. Y. Protein-directed synthesis of highly fluorescent gold nanoclusters. *J. Am. Chem. Soc.* **2009**, *131*, 888–889.

[66] Wang, C. S.; Li, J. Y.; Amatore, C.; Chen, Y.; Jiang, H.; Wang, X. M. Gold nanoclusters and graphene nanocomposites for drug delivery and imaging of cancer cells. *Angew Chem., Int. Ed.* **2011**, *50*, 11644–11648.

[67] Mohanty, P.; Park, J.; Lee, G.; Kim, B. Fabrication of single crystalline cadmium nanowires by a facile low temperature vapor phase method. *J. Nanosci. Nanotechnol.* **2006**, *6*, 3376–3379.

[68] Chaudhari, K.; Xavier, P. L.; Pradeep, T. Understanding the evolution of luminescent gold quantum clusters in protein templates. *ACS Nano* **2011**, *5*, 8816–8827.

[69] Nanda, J.; Kuruvilla, B. A.; Sarma, D. D. Photoelectron spectroscopic study of CdS nanocrystallites. *Phys. Rev. B* **1999**, *59*, 7473–7479.

[70] Peterson, M. D.; Jensen, S. C.; Weinberg, D. J.; Weiss, E. A. Mechanisms for adsorption of methyl viologen on CdS quantum dots. *ACS Nano* **2014**, *8*, 2826–2837.

[71] Trinh, T. T.; Mott, D.; Thanh, N. T. K.; Maenosono, S. One-pot synthesis and characterization of well defined core–shell structure of FePt@ CdSe nanoparticles. *RSC Adv.* **2011**, *1*, 100–108.

[72] Moholkar, A. V.; Agawane, G. L.; Sim, K.-U.; Kwon, Y.-B.; Choi, D. S.; Rajpure, K. Y.; Kim, J. H. Temperature dependent structural, luminescent and XPS studies of CdO: Ga thin films deposited by spray pyrolysis. *J. Alloys Compd.* **2010**, *506*, 794–799.

[73] Mohanty, J. S.; Xavier, P. L.; Chaudhari, K.; Bootharaju, M. S.; Goswami, N.; Pal, S. K.; Pradeep, T. Luminescent, bimetallic AuAg alloy quantum clusters in protein templates. *Nanoscale* **2012**, *4*, 4255–4262.

[74] Luo, Z. M.; Yang, D. L.; Qi, G. Q.; Shang, J. Z.; Yang, H. P.; Wang, Y. L.; Yuwen, L. H.; Yu, T.; Huang, W.; Wang, L. H. Microwave-assisted solvothermal preparation of nitrogen and sulfur co-doped reduced graphene oxide and graphene quantum dots hybrids for highly efficient oxygen reduction. *J. Mater. Chem. A* **2014**, *2*, 20605–20611.

[75] Makarova, A. A.; Grachova, E. V.; Neudachina, V. S.; Yashina, L. V.; Blüher, A.; Molodtsov, S. L.; Mertig, M.; Ehrlich, H.; Adamchuk, V. K.; Laubschat, C. et al. Insight into bio-metal interface formation *in vacuo*: Interplay of S-layer protein with copper and iron. *Sci. Rep.* **2015**, *5*, 8710.

[76] Wagner, A. J.; Wolfe, G. M.; Fairbrother, D. H. Reactivity of vapor-deposited metal atoms with nitrogen-containing polymers and organic surfaces studied by *in situ* XPS. *Appl. Surf. Sci.* **2003**, *219*, 317–328.

[77] Cho, K.; Wang, X.; Nie, S. M.; Chen, Z.; Shin, D. M. Therapeutic nanoparticles for drug delivery in cancer. *Clin. Cancer Res.* **2008**, *14*, 1310–1316.

[78] Zhang, C. L.; Li, C.; Liu, Y. L.; Zhang, J. P.; Bao, C. C.; Liang, S. J.; Wang, Q.; Yang, Y.; Fu, H. L.; Wang, K. et al.

Gold nanoclusters-based nanoprobes for simultaneous fluorescence imaging and targeted photodynamic therapy with superior penetration and retention behavior in tumors. *Adv. Funct. Mater.* **2015**, *25*, 1314–1325.

[79] Albanese, A.; Tang, P. S.; Chan, W. C. W. The effect of nanoparticle size, shape, and surface chemistry on biological systems. *Annu. Rev. Biomed. Eng.* **2012**, *14*, 1–16.

[80] Zhou, M.; Li, J. J.; Liang, S.; Sood, A. K.; Liang, D.; Li, C. CuS nanodots with ultrahigh efficient renal clearance for positron emission tomography imaging and image-guided photothermal therapy. *ACS Nano* **2015**, *9*, 7085–7096.

[81] Knop, K.; Hoogenboom, R.; Fischer, D.; Schubert, U. S. Poly(ethylene glycol) in drug delivery: Pros and cons as well as potential alternatives. *Angew. Chem., Int. Ed.* **2010**, *49*, 6288–6308.

[82] Song, E. Q.; Han, W. Y.; Li, C.; Cheng, D.; Li, L. R.; Liu, L. C.; Zhu, G. Z.; Song, Y.; Tan, W. H. Hyaluronic acid-decorated graphene oxide nanohybrids as nanocarriers for targeted and pH-responsive anticancer drug delivery. *ACS Appl. Mater. Interfaces* **2014**, *6*, 11882–11890.

[83] Yu, M. H.; Jambhrunkar, S.; Thorn, P.; Chen, J. Z.; Gu, W. Y.; Yu, C. Z. Hyaluronic acid modified mesoporous silica nanoparticles for targeted drug delivery to CD44-overexpressing cancer cells. *Nanoscale* **2013**, *5*, 178–183.

[84] Jayakumar, R.; Nair, A.; Rejinold, N. S.; Maya, S.; Nair, S. V. Doxorubicin-loaded pH-responsive chitin nanogels for drug delivery to cancer cells. *Carbohydr. Polym.* **2012**, *87*, 2352–2356.

[85] Zhou, Q.; Guo, X.; Chen, T.; Zhang, Z.; Shao, S. J.; Luo, C.; Li, J. R.; Zhou, S. B. Target-specific cellular uptake of folate-decorated biodegradable polymer micelles. *J. Phys. Chem. B* **2011**, *115*, 12662–12670.

[86] Palanikumar, L.; Choi, E. S.; Cheon, J. Y.; Joo, S. H.; Ryu, J. H. Noncovalent polymer-gatekeeper in mesoporous silica nanoparticles as a targeted drug delivery platform. *Adv. Funct. Mater.* **2015**, *25*, 957–965.